J. Fluid Mech. (2001), *vol.* 442, *pp.* 171–189. Printed in the United Kingdom

Expansion of a compressible gas bubble in Stokes flow

By C. POZRIKIDIS
Department of Mechanical and Aerospace Engineering, University of California, San Diego,
La Jolla, CA 92093-0411, USA
e-mail: cpozrikidis@ucsd.edu

(Received 16 October 2000 and in revised form 15 March 2001)

The flow-induced deformation of an inviscid bubble occupied by a compressible gas and suspended in an ambient viscous liquid is considered at low Reynolds numbers with particular reference to the pressure developing inside the bubble. Ambient fluid motion alters the bubble pressure with respect to that established in the quiescent state, and requires the bubble to expand or contract according to an assumed equation of state. When changes in the bubble volume are prohibited by a global constraint on the total volume of the flow, the ambient pressure is modified while the bubble pressure remains constant during the deformation. A numerical method is developed for evaluating the pressure inside a two-dimensional bubble in an ambient Stokes flow on the basis of the normal component of the interfacial force balance involving the capillary pressure, the normal viscous stress, and the pressure at the free surface on the side of the liquid; the last is computed by evaluating a strongly singular integral. Dynamical simulations of bubble deformation are performed using the boundary integral method properly implemented to remove the multiplicity of solutions due to the *a priori* unknown rate of expansion, and three particular problems are discussed in detail: the shrinkage of a bubble at a specified rate, the deformation of a bubble subject to simple shear flow, and the deformation of a bubble subject to a purely elongational flow. In the case of shrinkage, it is found that the surface tension plays a critical role in determining the behaviour of the bubble pressure near the critical time when the bubble disappears. In the case of shear or elongational flow, it is found that the bubble contracts during an initial period of deformation from the circular shape, and then it expands to obtain a stationary shape whose area is higher than that assumed in the quiescent state. Expansion may destabilize the bubble by raising the capillary number above the critical threshold under which stationary shapes can be found.

1. Introduction

The expansion, contraction, and collective interactions of bubbles consisting of a compressible gas and suspended in an ambient liquid have been studied extensively by previous authors with particular interest in regular and chaotic volume and shape oscillations, cavitation and collapse near rigid and deformable boundaries, and in the transport properties of bubbly liquids. Reviews can be found in the articles by Blake & Gibson (1987), Sangani & Didwania (1993), and Prosperetti (1999). The motion of the liquid is typically considered at high Reynolds numbers, and the effects of viscosity are neglected, taken into consideration through a global energy balance under the assumption of irrotational fluid motion (Sangani & Didwania 1993), or included in the formulation by means of a boundary-layer analysis for the vortex layer developing along the free surface (e.g. Boulton-Stone 1995). An exception occurs in the case of the radial oscillations of a perfectly spherical bubble where an exact solution of the equations of viscous flow underlying the generalized Rayleigh–Plesset equation can be found at any Reynolds number (e.g. Plesset & Prosperetti 1977).

Consider a solitary bubble containing a compressible gas, convected by, and possibly deforming under, the influence of an ambient viscous flow. The motion of the liquid causes the bubble pressure to change by an amount that depends on the type and strength of the ambient flow. In response, the bubble expands or contracts according to an equation of state appropriate for the gas occupying the bubble, and subject to the prevailing thermodynamic conditions requiring, for example, isothermal or adiabatic behaviour. Richardson (1968) derived exact solutions describing infinite shear or purely straining Stokes flow past a deformed two-dimensional bubble at steady state, and presented analytical expressions for the difference between the bubble pressure and the liquid pressure at infinity. Miksis (1981) used the boundary integral formulation to compute the shapes of axisymmetric bubbles in axisymmetric stagnation-point flow, and presented graphs relating the Weber number to the difference between the bubble pressure and the stagnation pressure occurring at the bubble surface on the axis of symmetry. The results of Richardson and Miksis, in conjuction with an assumed equation of state for the gas occupying the bubble, may be used to compute the volume or area of a deformed bubble and thus the capillary or Weber number and bubble shape at steady state using an iterative method, as will be discussed in §§ 5 and 6.

Several authors have used numerical methods based on the stream function–vorticity formulation to compute steady and unsteady axisymmetric flows past deformable inviscid gas bubbles at low and moderate Reynolds numbers (e.g. Ryskin & Leal 1984; Christov & Volkov 1985; Kang & Leal 1987; Takagi, Prosperetti & Matsumoto 1994; Yuan & Prosperetti 1994). In the case of steady flow, the bubble volume was specified and used to define the Reynolds number, Weber number, and capillary number. In the case of unsteady flow, it was assumed that the bubble volume is preserved during the motion. In the stream function–vorticity formulation, the bubble pressure does not need to be computed as part of the solution; instead, it may be evaluated *a posteriori* by solving the Poisson equation for the pressure in the liquid subject to Neumann boundary conditions that arise by projecting the equation of motion normal to the bubble surface, and then using the normal component of the interfacial force balance to relate the liquid to the bubble pressure at a chosen point.

Christov & Volkov (1985) considered steady streaming axisymmetric flow past a deformed bubble, and used the normal component of the interfacial condition for the traction over the bubble surface, involving the difference between the bubble pressure and the pressure at infinity, to compute the shape of the free surface by iteration. In their discussion of the numerical method, they note that the constraint on the bubble volume may be replaced by an equation of state for the gas occupying the bubble, but do not explore this possibility. Kang & Leal (1987) incorporated the bubble pressure into an un-named integration constant which is computed to ensure that the bubble volume remains constant during the deformation. To this author's knowledge, the flow-induced expansion or contraction of a bubble consisting of a compressible gas in viscous flow at small or moderate Reynolds numbers has not been discussed by previous authors.

In this paper, we consider the pressure developing inside an inviscid two-dimensional

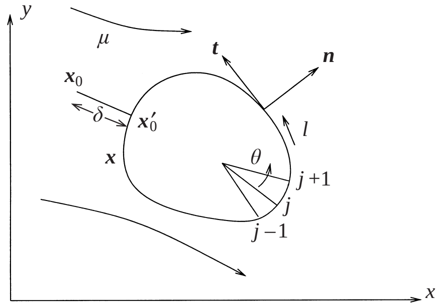

FIGURE 1. Illustration of Stokes flow past a two-dimensional inviscid bubble occupied by a compressible gas.

compressible bubble as a result of an ambient fluid motion under conditions of Stokes flow, and discuss the accompanying changes in the bubble volume. The velocity and pressure at the free surface are computed, respectively, by solving an integral equation subject to a constraint on the rate of change of the bubble area, and by evaluating a strongly singular integral representation. Consideration of the analogous and more realistic problem in three dimensions was prohibited by analytical and numerical difficulties in evaluating with sufficient accuracy the strongly singular integral representation for the pressure.

In the numerical method, the solution of the integral equation for the interfacial velocity is made unique by two alternative methods involving eigenvalue spectrum deflation or projection, and the strongly singular integral representation for the pressure is evaluated by reducing the order of the singularity using asymptotic methods. Numerical simulations of the deformation of a two-dimensional bubble illustrate the effect of bubble compressibility in three complementary types of flow discussed by Richardson (1968) and more recently by Tanveer & Vasconcelos (1995): shrinkage at a specified rate, deformation in shear flow, and deformation in a purely elongational flow.

2. Problem statement

Consider flow past a two-dimensional bubble suspended in a viscous liquid, as illustrated in figure 1. The bubble is occupied by a compressible gas whose viscosity is negligible compared to that of the liquid. The Reynolds number of the flow $Re = \rho a U/\mu$ is assumed to be so small that unsteady and nonlinear inertial forces are negligible, and the motion of the liquid is governed by the linear equations of Stokes flow; U is the characteristic velocity of the flow, a is the equivalent bubble radius defined such that the bubble area is πa^2, μ and ρ are the viscosity and density of the liquid. When gravitational forces are negligible, the motion of the liquid is governed by the equations of Stokes flow, including the continuity equation and the homogeneous Stokes equation

$$\nabla \cdot \boldsymbol{u} = 0, \quad -\nabla p + \mu \nabla^2 \boldsymbol{u} = \boldsymbol{0}, \tag{2.1}$$

where $\boldsymbol{u}$ is the velocity and p is the pressure.

The gas–liquid interface is assumed to be a free surface with uniform surface tension γ. The hydrodynamic traction along the free surface on the side of the liquid is then given by

$$\boldsymbol{f} \equiv \boldsymbol{\sigma} \cdot \boldsymbol{n} = (-p_B + \gamma\kappa)\boldsymbol{n}, \tag{2.2}$$

where $\boldsymbol{\sigma}$ is the Newtonian stress tensor, $\boldsymbol{n}$ is the unit vector normal to the free surface pointing into the liquid, p_B is the bubble pressure, and κ is the curvature of the free surface in the (x, y)-plane; for a circular bubble of radius a, $\kappa = 1/a$. As required by definition, the tangential component of the traction vanishes along the free surface.

If the liquid is stationary, the interface is circular, and the bubble pressure p_B is given by the Young–Laplace equation $p_B = p_\infty + \gamma\kappa$, where p_∞ is the uniform pressure of the liquid in the vicinity of the bubble. Fluid motion induces variations in the normal component of the traction exerted on the free surface on the side of the liquid, and causes the bubble to deform, and also expand or contract, in order to satisfy the normal free-surface balance

$$p_B = -\boldsymbol{n} \cdot \boldsymbol{\sigma} \cdot \boldsymbol{n} + \gamma\kappa, \tag{2.3}$$

where the bubble pressure p_B is assumed to be known from thermodynamics, as will be discussed in the next paragraph. In particular, the change in the bubble area A_B is determined by the instantaneous flow rate across the free surface given by

$$Q = \frac{\mathrm{d}A_B}{\mathrm{d}t} = \int_C \boldsymbol{u} \cdot \boldsymbol{n} \, \mathrm{d}l, \tag{2.4}$$

where C is the bubble surface. The flow rate Q is an unknown that must be computed as part of the solution in order to satisfy the normal force balance (2.3). This requirement effectively introduces an implicit constraint for determining the rate of bubble expansion or contraction at any time.

Now, the bubble pressure and area are related by an appropriate equation of state. For example, in the case of an ideal gas, the product $p_B A_B$ is equal to nRT, where n is the number of gram-moles comprising the gas, R is the ideal gas constant, and T is the absolute temperature. Assuming that the temperature of the bubble remains constant in time, we differentiate the ideal gas law with respect to time and obtain an evolution equation for the bubble pressure,

$$\frac{\mathrm{d}p_B}{\mathrm{d}t} = -\frac{p_B}{A_B} Q. \tag{2.5}$$

Similar evolution equations can be derived to describe the behaviour of the bubble pressure under adiabatic instead of isothermal conditions. Appending to equations (2.1)–(2.3) the evolution law (2.5), we obtain a complete system of equations governing the fluid motion and the bubble deformation. The system is to be solved subject to an initial condition that specifies the bubble shape, area, and pressure at the designated origin of time.

3. Integral formulation and numerical method

To compute the interfacial velocity and thereby track the deformation of the free surface, we use the boundary-integral formulation for Stokes flow and express the velocity at a point $\boldsymbol{x}_0$ that is located in the liquid in the integral form

$$u_j(\boldsymbol{x}_0) = u_j^\infty(\boldsymbol{x}_0) - \frac{1}{4\pi\mu} \int_C f_i(\boldsymbol{x}) G_{ij}(\boldsymbol{x}, \boldsymbol{x}_0) \, \mathrm{d}l(\boldsymbol{x}) + \frac{1}{4\pi} \int_C u_i(\boldsymbol{x}) T_{ijk}(\boldsymbol{x}, \boldsymbol{x}_0) n_k(\boldsymbol{x}) \, \mathrm{d}l(\boldsymbol{x}), \tag{3.1}$$

where $\boldsymbol{u}^\infty$ is the velocity of a specified incident flow, $\boldsymbol{f} \equiv \boldsymbol{\sigma} \cdot \boldsymbol{n}$ is the free-surface traction given in (2.2), and G_{ij} and T_{ijk} are the velocity and stress Green's functions of Stokes flow (e.g. Pozrikidis 1992). In the absence of boundaries, these are given by the free-space forms

$$G_{ij}(\boldsymbol{x}, \boldsymbol{x}_0) = -\delta_{ij} \ln r + \frac{\hat{x}_i \hat{x}_j}{r^2}, \quad T_{ijk}(\boldsymbol{x}, \boldsymbol{x}_0) = -4 \frac{\hat{x}_i \hat{x}_j \hat{x}_k}{r^4}, \tag{3.2a,b}$$

where $\hat{\boldsymbol{x}} = \boldsymbol{x} - \boldsymbol{x}_0$ is the distance of the integration point $\boldsymbol{x}$ from the evaluation point $\boldsymbol{x}_0$, and $r = |\hat{\boldsymbol{x}}|$.

The pressure is given by the corresponding integral representation

$$p(\boldsymbol{x}_0) = p^\infty(\boldsymbol{x}_0) - \frac{1}{4\pi} \int_C f_i(\boldsymbol{x}) P_i(\boldsymbol{x}_0, \boldsymbol{x}) \, \mathrm{d}l(\boldsymbol{x}) + \frac{\mu}{4\pi} \int_C u_i(\boldsymbol{x}) \Pi_{ik}(\boldsymbol{x}_0, \boldsymbol{x}) n_k(\boldsymbol{x}) \, \mathrm{d}l(\boldsymbol{x}), \tag{3.3}$$

where p^∞ is the pressure of the specified incident flow, and the kernels P_i and Π_{ik} are the pressure fields associated with the point force and the stresslet. For flow in free space,

$$P_i(\boldsymbol{x}_0, \boldsymbol{x}) = -2 \frac{\partial \ln r}{\partial \hat{x}_i} = -2 \frac{\hat{x}_i}{r^2}, \tag{3.4a}$$

$$\Pi_{ik}(\boldsymbol{x}_0, \boldsymbol{x}) = -4 \frac{\partial^2 \ln r}{\partial \hat{x}_i \partial \hat{x}_k} = -4 \frac{\delta_{ik}}{r^2} + 8 \frac{\hat{x}_i \hat{x}_k}{r^4}. \tag{3.4b}$$

If the flow is bounded by interior or exterior surfaces, the velocity and pressure Green's functions and the pressure kernels may be decomposed into the free-space components given in (3.2) and (3.4), and complementary components that are non-singular thoughout the domain of flow.

3.1. *Integral equation for the velocity*

Taking the limit as the point $\boldsymbol{x}_0$ approaches the free surface, and expressing the limit of the double-layer potential represented by the second integral on the right-hand side of (3.1) in terms of its principal value, we obtain an integral equation for the interfacial velocity,

$$u_j(\boldsymbol{x}_0) = u_j^\infty(\boldsymbol{x}_0) - \frac{1}{2\pi\mu} \int_C f_i(\boldsymbol{x}) G_{ij}(\boldsymbol{x}, \boldsymbol{x}_0) \, \mathrm{d}l(\boldsymbol{x}) + \frac{1}{2\pi} \int_C^{PV} u_i(\boldsymbol{x}) T_{ijk}(\boldsymbol{x}, \boldsymbol{x}_0) n_k(\boldsymbol{x}) \, \mathrm{d}l(\boldsymbol{x}), \tag{3.5}$$

where PV denotes the principal value. Previous authors have shown that the corresponding homogeneous equation

$$\psi_j(\boldsymbol{x}_0) = \frac{1}{2\pi} \int_C^{PV} \psi_i(\boldsymbol{x}) T_{ijk}(\boldsymbol{x}, \boldsymbol{x}_0) n_k(\boldsymbol{x}) \, \mathrm{d}l(\boldsymbol{x}) \tag{3.6}$$

admits a non-trivial eigensolution ψ that expresses the interfacial velocity established when the bubble expands or shrinks at an arbitrary rate due to a high or low internal pressure in the absence of surface tension (e.g. Pozrikidis 1992). The corresponding eigensolution of the adjoint equation

$$\phi_j(\boldsymbol{x}_0) = \frac{1}{2\pi} \int_C^{PV} \phi_i(\boldsymbol{x}) T_{jik}(\boldsymbol{x}_0, \boldsymbol{x}) n_k(\boldsymbol{x}_0) \, \mathrm{d}l(\boldsymbol{x}) \tag{3.7}$$

is the normal vector, $\phi_i = n_i$. Consequently, the integral equation (3.5) has a one-parameter family of solutions.

One way to remove the non-uniqueness of solution of the integral equation is to specify that the bubble area changes in time at a stipulated rate Q, and then add the term

$$z_j(\boldsymbol{x}_0)\left[\int_C u_i(\boldsymbol{x})n_i(\boldsymbol{x})\,\mathrm{d}l(\boldsymbol{x}) - Q\right] \tag{3.8}$$

to the right-hand side of (3.5), where $\boldsymbol{z}$ is an arbitrary function required to be non-orthogonal to ϕ_i, $\int_C z_i n_i \,\mathrm{d}l \neq 0$; an example is $z_i = \phi_i = n_i$. With this addition, the integral equation has a unique solution that satisfies the constraint (2.4). Since the introduction of the term (3.8) shifts the unit-norm eigenvalue of the double-layer potential, this method can be described as deflation.

Another way of removing the non-uniqueness of solution of the integral equation (3.5) originates from the solvability condition. In numerical practice, the integral equation is transformed into a linear system of algebraic equations of the form

$$\boldsymbol{z} = \boldsymbol{A}\cdot\boldsymbol{z} + \boldsymbol{b}, \tag{3.9}$$

using, for example, a collocation or a Galerkin method. In the collocation method, the vector $\boldsymbol{z}$ contains the x- and y-components of the velocity at the free-surface nodes. The components of the matrix $\boldsymbol{A}$ are defined in terms of the double-layer potential defined over boundary elements, and the vector $\boldsymbol{b}$ incorporates the first two terms on the right-hand side of (3.5). The occurrence of the eigensolution ψ_i suggests that the matrix $\boldsymbol{I} - \boldsymbol{A}$ is nearly singular, and the condition number increases as the numerical error is made smaller.

Now, the solvability condition for (3.5) requires that the sum of the first two terms on the right-hand side be orthogonal to the eigenfunction of the adjoint, $\phi_i = n_i$; that is, the integral of their product over C should vanish. In the discretized version of the problem expressed by (3.9), this integral is represented by the inner product of the vector $\boldsymbol{b}$ and a vector $\boldsymbol{w}$ whose elements are defined in terms of integration weights that depend on the particular method selected for carrying out the integration. Because of discretization and integration error, the inner product $\boldsymbol{b}\cdot\boldsymbol{w}$ will not be equal to zero to machine precision.

To ensure that the linear system shares the properties of its ancestral integral equation regarding uniqueness of solution and solvability, we project both sides of (3.9) onto the space that is orthogonal to $\boldsymbol{w}$, thereby obtaining the singular system

$$\boldsymbol{B}\cdot\boldsymbol{z} = \boldsymbol{c}, \tag{3.10}$$

where $\boldsymbol{B} \equiv \boldsymbol{P}\cdot(\boldsymbol{I}-\boldsymbol{A})$, $\boldsymbol{c} \equiv \boldsymbol{P}\cdot\boldsymbol{b}$, and the matrix $\boldsymbol{P} \equiv \boldsymbol{I}-\boldsymbol{w}\boldsymbol{w}/|\boldsymbol{w}|^2$ carries out the projection. Clearly, the vector $\boldsymbol{w}$ is an eigenvector of the transpose of $\boldsymbol{B}$ corresponding to the zero eigenvalue, the solvability condition $\boldsymbol{w}\cdot\boldsymbol{c} = 0$ is fulfilled to machine precision, the coefficient matrix of the linear system (3.10) is rank-one deficient, and the system has a one-parameter family of solutions. One of the components of the unknown vector $\boldsymbol{z}$ may then be assigned an arbitrary value, and one equation of the linear system may be discarded and replaced by a constraint on the rate of expansion expressed by a discrete form of (2.4).

The two methods of solving the integral equation subject to a specified rate of expansion, based on deflation or projection, were implemented using a standard collocation method. The numerical procedure involves the following steps: (a) the free surface is traced with a set of Lagrangian marker points or nodes, and the shape of the free surface between two successive nodes is interpolated with blended circular arcs; (b) the velocity components along the free surface between two successive nodes are approximated with linear functions with respect to arc length; (c) the integral equation is applied at the nodes to yield a system of linear equations for the node velocities; (d) the linear system is solved by the method of Gauss elimination; (d) the position of the marker points is advanced in time using the second-order Runge–Kutta method with a constant time step. After a time step has been completed, the marker points are redistributed adaptively to ensure adequate spatial resolution and capture the development of regions of high curvature.

To compare the performance of the two methods, we consider the velocity along the free surface of an elliptical bubble with axes ratio 2 : 1, expanding at a specified rate Q in the absence of surface tension. Using the numerical method based on deflation, we find that the x-component of the free-surface velocity at a point on the x-axis is given by $u_x a/Q = 0.0899, 0.0900$ and 0.0900, respectively, for 32, 64, and 128 marker points, where a is the equivalent bubble radius. The corresponding velocity obtained with the projection method is 0.0902, 0.0901, 0.0900. This comparison suggests that the two methods are comparable in accuracy, with the first method having a slight but likely fortuitous advantage.

3.2. *Computation of the bubble pressure*

Suppose that the interfacial velocity field has been obtained using the numerical methods discussed in §3.1. To compute the bubble pressure, we use the normal component of the interfacial force balance expressed by equation (2.3) evaluated at a point at the free surface. Decomposing the normal stress into its pressure and viscous components, and using the continuity equation to express the viscous component in terms of the tangential derivative of the tangential velocity, we obtain

$$p_B = p + 2\mu \frac{\partial \boldsymbol{u}}{\partial l} \cdot \boldsymbol{t} + \gamma \kappa, \tag{3.11}$$

where $\boldsymbol{t}$ is the unit vector tangent to C pointing in the direction of increasing arc length l, as illustrated in figure 1. The second term on the right-hand side of (3.11) may be computed readily from knowledge of the interfacial velocity by numerical differentiation.

To evaluate the pressure at the free surface on the side of the liquid, we consider the limit of the right-hand side of the integral representation (3.3) as the point $\boldsymbol{x}_0$ approaches the free surface C. In this limit, the two integrals on the right-hand side become improper, exhibiting, respectively, a $1/r$ and an apparent $1/r^2$ singularity, as displayed in expressions (3.4). The former is classified as a principal-value integral, and the latter as a hypersingular integral. To compute the limiting values of these integrals, we first reduce the order of the singularities by substituting the interfacial condition (2.2) into the first integral on the right-hand side of (3.3), and then using integral identities to find that, in the limit as $\boldsymbol{x}_0$ tends to the bubble contour C, the pressure is given by

$$p(\boldsymbol{x}_0) = p^{\infty}(\boldsymbol{x}_0) - \frac{\gamma}{4\pi} \int_C n_i(\boldsymbol{x}) P_i(\boldsymbol{x}_0, \boldsymbol{x}) [\kappa(\boldsymbol{x}) - \kappa(\boldsymbol{x}_0)] \, \mathrm{d}l(\boldsymbol{x}) + \frac{\mu}{4\pi} \int_C [u_i(\boldsymbol{x}) - u_i(\boldsymbol{x}_0)] \Pi_{ik}(\boldsymbol{x}_0, \boldsymbol{x}) n_k(\boldsymbol{x}) \, \mathrm{d}l(\boldsymbol{x}). \tag{3.12}$$

The order of the singularity has been reduced by one unit in both integrals.

Inspection of the free-space pressure kernel P_i given in (3.4*a*) shows that the kernel of the first integral on the right-hand side of (3.12) remains regular as the evaluation point $\boldsymbol{x}_0$ approaches and then crosses the domain of integration C. When, in particular, $\boldsymbol{x}_0$ is located on C, as the integration point $\boldsymbol{x}$ tends to the evaluation point $\boldsymbol{x}_0$, the distance $\hat{\boldsymbol{x}}$ tends to become perpendicular to the normal vector $\boldsymbol{n}$, the product $n_i(\boldsymbol{x})P_i(\boldsymbol{x}_0, \boldsymbol{x})$ tends to a finite limit, and the first integrand in (3.12) tends to vanish.

The computation of the second integral on the right-hand side of (3.12) is more subtle. Substituting into the integrand the free-space kernel given in (3.4*b*), and decomposing the integral into two parts, we obtain

$$\int_C [u_i(\boldsymbol{x}) - u_i(\boldsymbol{x}_0)]\Pi_{ik}(\boldsymbol{x}_0, \boldsymbol{x})n_k(\boldsymbol{x})\,\mathrm{d}l(\boldsymbol{x}) = -4\int_C [u_i(\boldsymbol{x}) - u_i(\boldsymbol{x}_0)]\frac{n_i(\boldsymbol{x})}{r^2}\,\mathrm{d}l(\boldsymbol{x}) \\ +8\int_C [u_i(\boldsymbol{x}) - u_i(\boldsymbol{x}_0)]\frac{\hat{x}_i\hat{x}_k}{r^4}n_k(\boldsymbol{x})\,\mathrm{d}l(\boldsymbol{x}). \quad (3.13)$$

To compute the first integral on the right-hand side of (3.13) in the limit as the evaluation point $\boldsymbol{x}_0$ approaches C, we consider the projection of $\boldsymbol{x}_0$ onto C, denoted by $\boldsymbol{x}'_0$, as illustrated in figure 1. Using Taylor series expansions, we write

$$u_i(\boldsymbol{x}_0) = u_i(\boldsymbol{x}'_0) + \left(\frac{\partial u_i}{\partial l_n}\right)_{\boldsymbol{x}'_0} \delta + \cdots, \quad (3.14)$$

where l_n is the arc length measured in the direction of the normal vector $\boldsymbol{n}$, and $\delta = |\boldsymbol{x}_0 - \boldsymbol{x}'_0|$. Considering also a point $\boldsymbol{x}$ that lies on C in the vicinity of the free-surface point $\boldsymbol{x}'_0$, we write the analogous expansion

$$u_i(\boldsymbol{x}) = u_i(\boldsymbol{x}'_0) + \left(\frac{\partial u_i}{\partial l}\right)_{\boldsymbol{x}'_0} (l - l'_0) + \cdots, \quad (3.15)$$

where l is the arc length along C measured in the direction of the tangent vector $\boldsymbol{t}$, and $l'_0 \equiv l(\boldsymbol{x}'_0)$. Substituting (3.14) and (3.15) into the first integral on the right-hand side of (3.13), we express it in the form

$$-4\left(\frac{\partial u_i}{\partial l}\right)_{\boldsymbol{x}'_0} n_i(\boldsymbol{x}'_0)\int_C \frac{l - l'_0}{\delta^2 + (l - l'_0)^2}\mathrm{d}l(\boldsymbol{x}) \\ +4\left(\frac{\partial u_i}{\partial l_n}\right)_{\boldsymbol{x}'_0} n_i(\boldsymbol{x}'_0)\int_C \frac{\delta}{\delta^2 + (l - l'_0)^2}\mathrm{d}l(\boldsymbol{x}) + \cdots, \quad (3.16)$$

where the dots represent contributions that are finite and continuous throughout the domain of flow. In the limit as δ tends to zero, the first integral of (3.16) becomes a Cauchy principal-value integral, and the second integral tends to the finite value of π.

Turning now to the second integral on the right-hand side of (3.13), we express it in the form

$$8\int_C \left[u_i(\boldsymbol{x}) - u_i(\boldsymbol{x}_0) - \left(\frac{\partial u_i}{\partial x_j}\right)_{\boldsymbol{x}'_0} \hat{x}_j\right] \frac{\hat{x}_i\hat{x}_k}{r^4}n_k(\boldsymbol{x})\,\mathrm{d}l(\boldsymbol{x}) \\ -2\left(\frac{\partial u_i}{\partial x_j}\right)_{\boldsymbol{x}'_0} \int_C \left[-4\frac{\hat{x}_i\hat{x}_j\hat{x}_k}{r^4}\right] n_k(\boldsymbol{x})\,\mathrm{d}l(\boldsymbol{x}). \quad (3.17)$$

Because the first integrand is non-singular, the corresponding integral remains continuous as the evaluation point $\boldsymbol{x}_0$ approaches and then crosses C. Identifying the integrand of the second integral with the stress Green's function T_{ijk} given in (3.2*b*), using the integral identity $\int_C T_{ijk} n_k \, \mathrm{d}l = 0$ when $\boldsymbol{x}_0$ is exterior to C, or $-\frac{1}{2}\delta_{ij}$ when $\boldsymbol{x}_0$ is on C, and invoking the continuity equation to set $\partial u_i/\partial x_i = 0$, we conclude that, in the limit as $\boldsymbol{x}_0$ tends to C, the second integral on the right-hand side of (3.13) tends to the value of the integral computed when $\boldsymbol{x}_0$ lies on C. We note, once again, that, when $\boldsymbol{x}_0$ is on C, as the integration point $\boldsymbol{x}$ tends to the evaluation point $\boldsymbol{x}_0$ the distance $\hat{\boldsymbol{x}} \equiv \boldsymbol{x} - \boldsymbol{x}_0$ tends to become perpendicular to the normal vector $\boldsymbol{n}$, and find that the integrand is non-singular and may be evaluated using a standard numerical method. Similar results are obtained by analysing the behaviour of the second integral on the right-hand side of (3.13) in terms of the expansions (3.14) and (3.15).

Combining the preceding results, and using the continuity equation to write $(\partial u_i/\partial l_n) n_i = -(\partial u_i/\partial l) t_i$, we find that the pressure at the point $\boldsymbol{x}_0$ that lies at the free surface on the side of the liquid is given by the regularized integral representation

$$
\begin{aligned}
p(\boldsymbol{x}_0) = p^{\infty}(\boldsymbol{x}_0) &+ \frac{\gamma}{2\pi} \int_C n_i(\boldsymbol{x}) \frac{x_i - x_{0_i}}{r^2} [\kappa(\boldsymbol{x}) - \kappa(\boldsymbol{x}_0)] \, \mathrm{d}l(\boldsymbol{x}) \\
&+ \frac{2\mu}{\pi} \int_C [u_i(\boldsymbol{x}) - u_i(\boldsymbol{x}_0)] \frac{\hat{x}_i \hat{x}_k}{r^4} n_k(\boldsymbol{x}) \, \mathrm{d}l(\boldsymbol{x}) \\
&- \frac{\mu}{\pi} \int_C^{PV} [u_i(\boldsymbol{x}) - u_i(\boldsymbol{x}_0)] \frac{n_i(\boldsymbol{x})}{r^2} \mathrm{d}l(\boldsymbol{x}) - \mu \left(\frac{\partial u_i}{\partial l} \right) (\boldsymbol{x}_0) t_i(\boldsymbol{x}_0), \qquad (3.18)
\end{aligned}
$$

where $\boldsymbol{x}_0$ is on C. The first two integrals on the right-hand side of (3.18) are non-singular, and the third integral is a Cauchy principal-value integral. The last term on the right-hand side of (3.18) may be computed from knowledge of the interfacial velocity by numerical differentiation.

To compute the Cauchy principal-value integral on the right-hand side of (3.18) when the evaluation point $\boldsymbol{x}_0$ is the jth node, we approximate the section of the free-surface between the marker points numbered $j-1$ and $j+1$ with a circular arc of radius a_j passing through these two points and through the intermediate jth point, as illustrated in figure 1. We then regard the Cartesian components of the velocity over the jth arc as functions of the polar angle θ measured in the counterclockwise direction around the arc centre, describe them by parabolic interpolation, and recast the Cauchy principal-value integral over the jth arc into the form

$$
\begin{aligned}
&\int_{A_j} \left[[u_i(\boldsymbol{x}) - u_i(\boldsymbol{x}_0)] \frac{n_i(\boldsymbol{x})}{r^2} - \left(\frac{\partial u_i}{\partial \theta} \right)_{\theta_j} (\theta - \theta_j) \frac{n_i(\boldsymbol{x}_0)}{a_j^2 (\theta - \theta_j)^2} \right] \mathrm{d}l(\boldsymbol{x}) \\
&\qquad\qquad \pm \frac{1}{a_j} \left(\frac{\partial u_i}{\partial \theta} \right)_{\theta_j} n_i(\boldsymbol{x}_0) \int_{A_j}^{PV} \frac{\mathrm{d}\theta}{\theta - \theta_j}, \qquad (3.19)
\end{aligned}
$$

where A_j stands for the jth arc, and the plus or minus sign in the last term applies, respectively, when the arc is traced in the counterclockwise or clockwise direction with respect to the distribution of the marker points. The first integral on the right-hand side of (3.19) is non-singular. The second principal-value integral may be computed by elementary analytical methods.

To assess the performance of the numerical method for evaluating the pressure, we used the integral representation (3.18) in conjunction with the boundary condition (3.11) to evaluate the bubble pressure at marker points distributed around the free surface of an elliptical bubble with axes ratio 2 : 1, where the bubble is shrinking

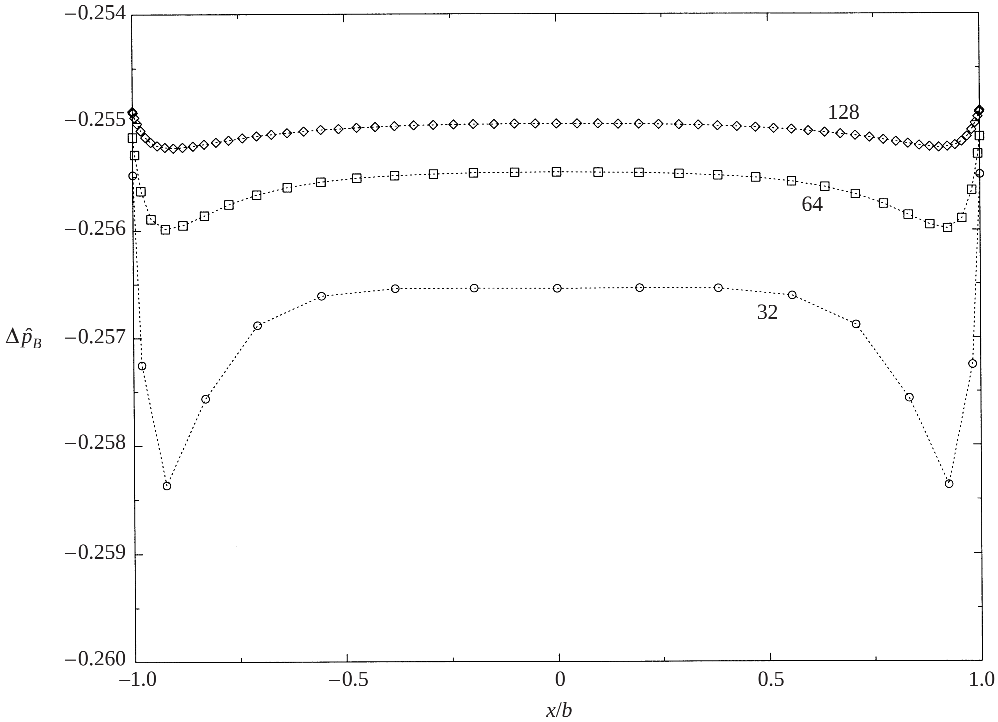

FIGURE 2. Distribution of the bubble pressure around the free surface of a shrinking elliptical bubble with axes ratio 2 : 1 computed from the integral representation (3.12) for several discretization levels.

at the specified areal rate Q. Figure 2 shows the distribution of the reduced bubble pressure $\Delta\hat{p}_B \equiv (p_B - p_\infty)a^2/(\mu|Q|)$ around half the free surface plotted against x/b, computed with 32, 64, and 128 marker points; a is the equivalent bubble radius, and b is the major semi-axis of the ellipse along the x-axis. In the absence of numerical error, the distribution of the bubble pressure should be uniform and independent of the evaluation point.

The numerical results displayed in figure 2 suggest that the bubble pressure converges at a linear rate with respect to the number of marker points. For 128 points, the maximum numerical error is estimated to be less than 1% of the exact value. This amount of error was also confirmed by comparing numerical with exact values, as will be discussed in subsequent sections. In view of well-known difficulties in evaluating hypersingular integrals (e.g. Sladek & Sladek 1998), a numerical error of this order is satisfactory. In the results presented in the remainder of this paper, the bubble pressure was computed as the average of the pointwise pressure evaluated at all marker points.

3.3. *Computation of the rate of expansion*

The linearity of the governing equations of Stokes flow with respect to velocity and pressure suggests that, at any instant, the bubble pressure is a linear function of the rate of expansion Q, and may thus be expressed in the form

$$p_B(Q) = p_B(Q = 0) + \alpha Q, \tag{3.20}$$

where α is a proportionality coefficient dependent on the instantaneous bubble shape. If the bubble pressure is specified and α is known, equation (3.20) may be used

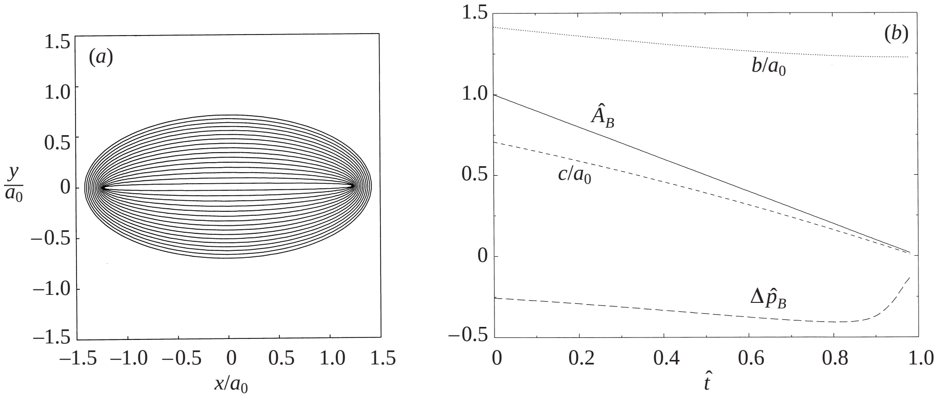

FIGURE 3. (*a*) Shrinkage of an elliptical bubble with initial axes ratio 2 : 1 at a specified negative rate of expansion Q in the absence of surface tension; free-surface profiles at dimensionless times $\hat{t} \equiv t|Q|/a_0^2 = 0, 0.20, 0.40, \ldots$, where a_0 is the initial equivalent radius. (*b*) Evolution of the bubble area reduced by the initial value, $\hat{A}_B$ (solid line), reduced major axis $\hat{b} \equiv b/a_0$ (dotted line), reduced minor axis $\hat{c} \equiv c/a_0$ (dashed line), and relative bubble pressure $\Delta\hat{p}_B \equiv (p_B - p_\infty)a_0^2/(\mu|Q|)$ (long dashed line).

to compute the rate of expansion. In the numerical implementation, the coefficient α was computed by the method of impulses based on the equation $\alpha = p_B(Q = 1) - p_B(Q = 0)$, where the bubble pressure is evaluated using the numerical method discussed in § 3.2. The rate of expansion was subsequently determined from the equation $Q = (p_B - p_B(Q = 0))/\alpha$.

4. Shrinkage of an elliptical bubble

Tanveer & Vasconcelos (1995) combined the complex-variable formulation of Stokes flow with conformal mapping to study the evolution of a two-dimensional bubble expanding or shrinking, respectively, at a specified positive or negative rate of expansion Q. Their results showed that expansion tends to restore the circular shape even in the absence of surface tension, whereas shrinkage may lead to the spontaneous formation of near-cusps at the free surface for a certain class of initial shapes. As a first case study, we consider the evolution of an initially elliptical bubble shrinking at a constant negative rate of expansion, compare the numerical results with the predictions of Tanveer & Vasconcelos (1995), and discuss the behaviour of the bubble pressure during the contraction.

Figure 3(*a*) shows successive stages in the evolution of the free surface of an elliptical bubble with initial axes ratio 2 : 1 in the absence of surface tension, simulated with 128 marker points around the interface. The numerical results are in excellent agreement with the predictions of Tanveer & Vasconcelos (1995): the bubble shrinks while maintaining an elliptical shape whose eccentricity increases monotonically in time. The solid line in figure 3(*b*) shows the evolution of the bubble area reduced by the initial value, plotted with respect to reduced time $\hat{t} \equiv t/t_{cr}$, where $t_{cr} = \pi a_0^2/|Q|$ is the critical time when the bubble disappears, and a_0 is the initial equivalent radius. The dotted and dashed lines illustrate the evolution of the major and minor axis of the elliptical interface, denoted by b and c, reduced by the initial equivalent bubble radius a_0. Tanveer & Vasconcellor (1995) predict that, at the critical time when the bubble disappears, the major axis b tends to the asymptotic value $\sqrt{b_0^2 - c_0^2} = \sqrt{1.5}a_0 =$

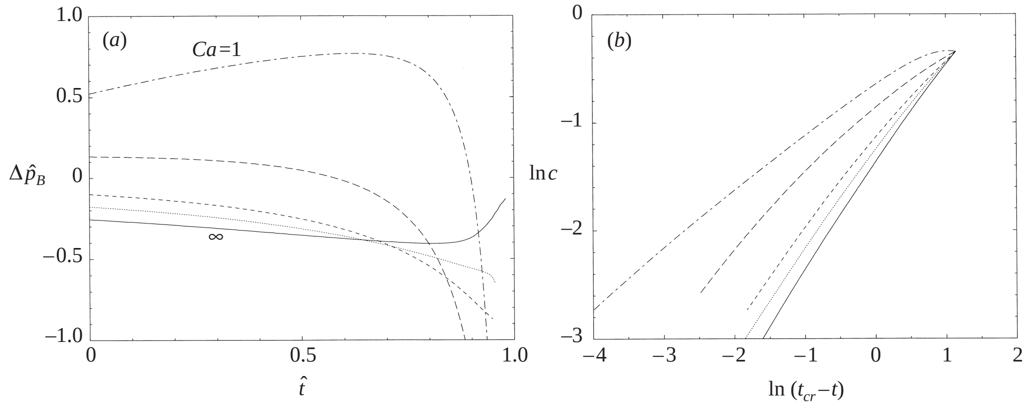

FIGURE 4. (*a*) Evolution of the relative bubble pressure during the shrinkage of an elliptical bubble with initial axes ratio 2 : 1 for initial capillary numbers $Ca_0 \equiv \mu|Q|/(a_0\gamma) = \infty$, 10, 5, 2, and 1. (*b*) Evolution of the minor bubble axis c plotted with respect to shifted time $t_{cr} - t$ on a log-log scale.

$1.225a_0$, while the minor axis tends to vanish, yielding an elongated bubble in the form of a narrow slit; the subscript 0 indicates the initial value. Our numerical results reproduce this behaviour and recover the asymptotic value of the major axis at the critical time accurate to the third significant figure.

The long-dashed line near the bottom of figure 3(*b*) shows the evolution of the reduced bubble pressure $\Delta\hat{p}_B \equiv (p_B - p_\infty)a_0^2/(\mu|Q|)$. The results reveal that the bubble pressure is less than the pressure at infinity, as required on physical grounds for the bubble to shrink in the absence of surface tension. Moreover, the results suggest that, as time approaches the critical time where the bubble disappears, $\Delta\hat{p}_B$ passes through a minimum and then it increases toward the value of zero. In contrast, the pressure inside a perfectly circular bubble of radius $a(t)$ shrinking at a constant negative rate Q is given by $p_B = p_\infty - \mu|Q|/(\pi a^2) + \gamma/a$. No matter how large the surface tension and associated capillary pressure, viscous stresses cause the bubble pressure to tend to negative infinity at the critical time where the bubble disappears.

In the absence of surface tension, and only then, the evolution of the free surface is independent of the functional form of the rate of expansion $Q(t)$, which merely serves to determine the rate by which the free surface passes through a continuous family of elliptical shapes. Tanveer & Vasconcelos (1995) predict that surface tension does not have a profound effect on the nature of the motion of the elliptical bubble, and its main effect is to modify the length of the slit-like bubble at the critical time where the bubble disappears. The results of our simulations corroborate these predictions. To illustrate the effect of surface tension on the bubble pressure, in figure 4(*a*) we display the evolution of the pressure difference $\Delta\hat{p}_B$ for initial capillary numbers $Ca_0 \equiv \mu|Q|/(a_0\gamma) = \infty$, 10, 5, 2, and 1. The results suggest that infinite capillary number is a special case: when the surface tension is non-zero, the bubble pressure tends to negative infinity at the critical time. Physically, the singular behaviour is attributed to strong viscous stresses developing at the tip of the shrinking ellipse during the final stages of collapse.

Because the capillary pressure over the flat side of a highly eccentric elliptical bubble is negligible, the singular bubble pressure developing in the presence of surface tension, illustrated in figure 4(*a*), must be balanced by the viscous normal stress. We note that the viscous stress over the flat side of the bubble scales with the y-component of the velocity evaluated at the free surface, denoted by v, and this requires that, near the critical time when the bubble disappears, v should diverge, and the upper and lower sides of the slit-like bubble will slam against each other at infinite speed. This behaviour is supported by the results presented in figure 4(*b*), illustrating the evolution of the bubble minor axes c with respect to shifted time $t_{cr} - t$, plotted on a log-log scale for several capillary numbers. The results suggest the power-law relation $c \equiv (t_{cr} - t)^{\beta}$, where β is close unity for infinite capillary number corresponding to zero surface tension, and less than unity for finite capillary numbers. We note that $\mathrm{d}c/\mathrm{d}t = v$, and this confirms the aforementioned singular behaviour in the presence of surface tension.

5. A bubble in simple shear flow

In the second case study, we consider the deformation of a bubble suspended in an ambient liquid of infinite expanse undergoing simple shear flow along the x-axis. Far from the bubble, the velocity is given by $\boldsymbol{u}^{\infty} = (ky, 0)$, where k is the shear rate, and the pressure is uniform. Richardson (1968) showed that it is possible for the bubble to deform and assume a steady shape, no matter how high the shear rate or how small the surface tension; that is, no matter how large the capillary number. The deformed shape is perfectly elliptical with major axis inclined with respect to the direction of the shear flow by a certain angle.

In the absence of fluid motion, the bubble has a circular shape, and the bubble pressure is given by the Young–Laplace law $p_{B_0} = p_{\infty} + \gamma/a_0$, where p_{∞} is the pressure outside the bubble, and a_0 is the bubble radius. Fluid motion causes the bubble pressure to change by an amount that depends on the shear rate, and the bubble area to undergo a corresponding change determined by an equation of state appropriate for the gas occupying the bubble. When the bubble has deformed and reached a steady state, the bubble pressure p_{B_s} and area A_s, where the subscript s denotes the steady state, are different from the initial values p_{B_0} and $A_0 = \pi a_0^2$. The change in bubble pressure $\delta p_B \equiv p_{B_s} - p_{B_0}$, the corresponding change in the bubble area $\delta A_B \equiv A_s - A_0$, and the bubble deformation and inclination at steady state, are all functions of the *a priori* unknown capillary number at steady state $Ca_s = \mu k a_s/\gamma$, and thus depend on the initial capillary number $Ca_o = \mu k a_0/\gamma$ and on the bubble gas equation of state.

Richardson (1968) provided analytical expressions for the bubble axes ratio, orientation, and pressure at steady state. The deformation parameter $D \equiv (A - B)/(A + B)$, where A and B are the major and minor axes of the deformed elliptical shape, satisfies the nonlinear algebraic equation

$$Ca_s - \frac{2}{\pi} D F(D) = 0, \tag{5.1}$$

where F is the complete elliptic integral of the first kind. The bubble inclination angle ϕ is related to the deformation parameter by the equation $D = \cos(2\phi)$, and the reduced bubble pressure $\Delta\hat{p}_{B_s} \equiv (p_{B_s} - p_{\infty})/(\mu k)$ is given by $\Delta\hat{p}_{B_s} = \sqrt{1 - D^2}/D$. As the capillary number is raised, the deformation parameter D tends to unity, and $\Delta\hat{p}_{B_s}$ tends to vanish.

In figure 5, we plot with the solid, dotted, and dashed line, respectively, D, ϕ, and the incremental change in the reduced bubble pressure defined as $\delta\hat{p}_B \equiv (p_{B_s} - p_{B_0})/(\mu k) = \Delta\hat{p}_{B_s} - 1/Ca_s$, against the capillary number Ca_s. The circle represents the results of a

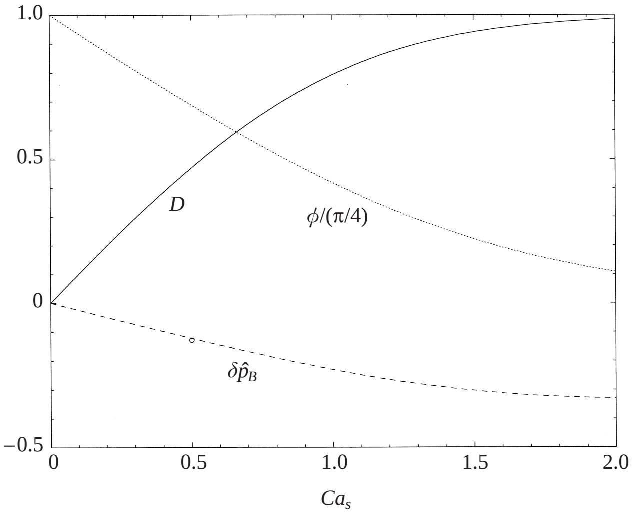

FIGURE 5. A bubble in simple shear flow; graphs of the Taylor deformation parameter D (solid line), bubble inclination ϕ (dotted line), and bubble pressure rise $\delta \hat{p}_B$ (dashed line) plotted against the capillary number at steady state.

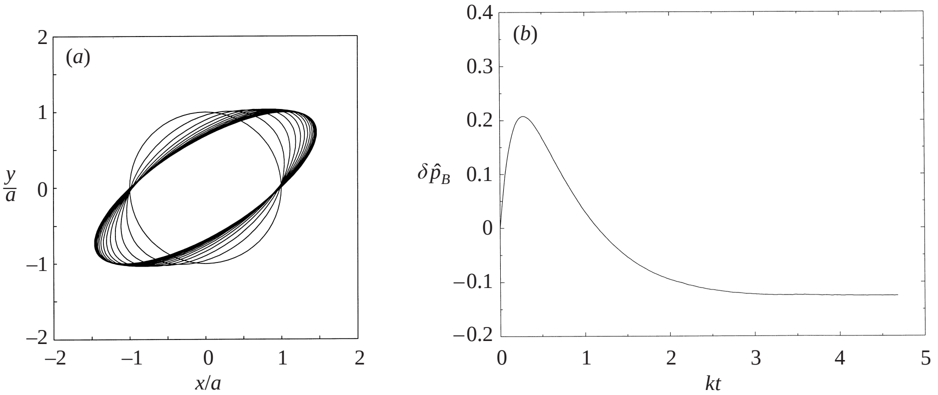

FIGURE 6. (a) Stages in the deformation of an incompressible bubble in simple shear flow, for capillary number $Ca_0 = Ca_s = \mu k a/\gamma = 2.0$; (b) corresponding evolution of the change in the bubble pressure expressed by $\delta \hat{p}_B$.

numerical simulation to be discussed later in this section. The dashed line in figure 5 suggests that the shear flow causes a reduction in the bubble pressure. Consequently, the bubble is expected to expand as it deforms to obtain the steady elliptical shape. Figure 5 may be used to compute the *a priori* unknown capillary number Ca_s, and thus the size and shape of the bubble at steady state, using an iterative method according to the following steps: assume that $Ca_s = Ca_0$, that is, the bubble area does not change due to the flow; read from figure 5 the corresponding bubble pressure; compute the bubble area from the bubble pressure using an appropriate equation of state for the gas occupying the bubble; recompute Ca_s based on the improved bubble area; repeat until convergence.

Tanveer & Vasconcelos (1995) showed that the transient deformation of an incompressible circular bubble occurs through a sequence of evolving elliptical shapes,

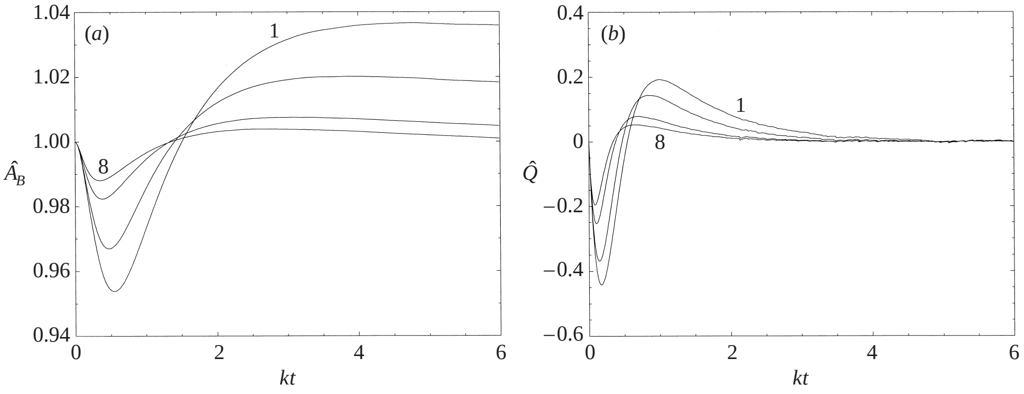

FIGURE 7. (*a*) Evolution of the area of a compressible bubble in simple shear flow, for $Ca_0 = 0.5$ and $\hat{p}_\infty = 1, 2, 5$, and 8. (*b*) Corresponding evolution of the reduced rate of expansion $\hat{Q} \equiv Q/(ka_0^2)$.

and derived a system of ordinary differential equations governing the evolution of the bubble axes ratio and orientation. Because of the constraint of constant area, the bubble pressure changes during the deformation. Figure 6(*a*) shows a sequence of stages in the deformation of an incompressible bubble for capillary number $Ca_0 = Ca_s = \mu k a_0/\gamma = 0.5$, computed using the boundary integral method, and figure 6(*b*) shows the evolution of the incremental bubble pressure expressed by $\delta \hat{p}_B$, computed using the numerical method discussed in § 3.2. The results show that the change in the bubble pressure is positive during the initial period of deformation, indicating that the bubble will shrink. The pressure then passes through a maximum, and finally becomes negative and tends to the asymptotic value represented by the circle in figure 5, indicating that the bubble will undergo a net expansion at steady state.

To confirm these predictions, we carried out a series of simulations on the transient deformation of a compressible bubble, where the evolution of the bubble area is determined from the bubble pressure according to the equation of state for an ideal gas under isothermal conditions, as discussed in § 2. The deformation of the bubble is a function of the initial capillary number $Ca_0 = \mu k a_0/\gamma$ and of the bubble pressure at the initial instant determined by the reduced pressure at infinity $\hat{p}_\infty = p_\infty a_0/\gamma$; in terms of $\hat{p}_\infty$, the initial bubble pressure is given by $p_{B_0} = a_0(1 + \hat{p}_\infty)/\gamma$. For a circular air bubble of radius 1 mm suspended in a liquid at atmospheric pressure, $\hat{p}_\infty$ is on the order of 10^3.

Figure 7(*a*) shows the evolution of the bubble area reduced by the initial area, $\hat{A}_B \equiv A_B/A_{B_0}$, for $Ca_0 = 0.5$ and $\hat{p}_\infty = 1, 2, 5$, and 8. The results confirm that the bubble initially shrinks and then expands to occupy an area that is larger than the initial value. The asymptotic increase in the bubble size is inversely proportional to the initial bubble pressure. For $\hat{p}_\infty = 1$, the bubble area at steady state is higher by 4% than the initial value; correspondingly, the capillary number at steady state is larger by 2% than the initial value. Although noticeable, this increase is not large enough for the compressibility of the bubble to have a significant effect on the overall bubble behaviour. Figure 7(*b*) shows the evolution of the reduced rate of expansion $\hat{Q} \equiv Q/(ka_0^2)$, suggesting that the rate of expansion decays to zero at a seemingly exponential rate at long times.

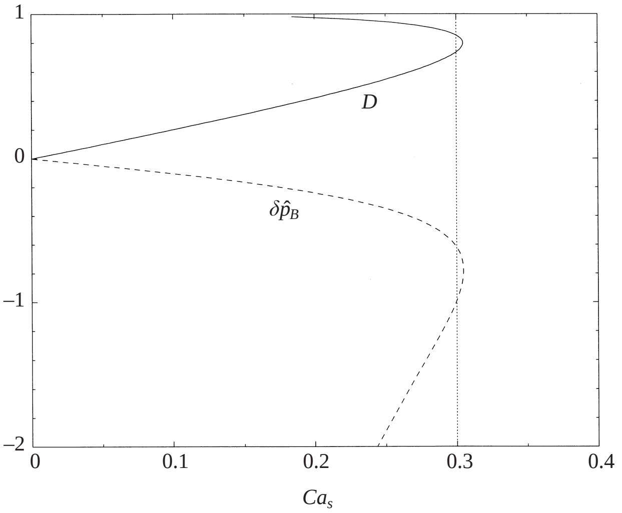

FIGURE 8. A bubble in purely elongational flow: graphs of the Taylor deformation parameter D (solid line), and bubble pressure rise $\delta\hat{p}_B$ (dashed line), plotted against the capillary number at steady state.

6. A bubble in purely straining flow

In the third case study, we consider the deformation of a bubble subject to a purely straining flow. Far from the bubble, the velocity field is given by $\boldsymbol{u}^\infty = (kx, -ky)$, where k is the rate of extension, and the pressure is uniform. Richardson (1968) demonstrated the existence of a critical value of the steady-state capillary number, $Ca_s = \mu k a_s/\gamma$, approximately equal to 0.305, above which a steady shape cannot be found. Below this critical value, the bubble may assume one of two possible elliptical shapes. The shape with the higher aspect ratio is unstable and may not be realized in practice.

Richardson (1968) provided analytical expressions for the Taylor deformation parameter, D, and reduced bubble pressure $\Delta\hat{p}_{B_s} \equiv (p_{B_s} - p_\infty)/(\mu k)$, at steady state. The former satisfies the algebraic equation

$$Ca_s - \frac{1}{\pi} D\sqrt{1-D^2}F(D) = 0, \tag{6.1}$$

where F is the complete elliptic integral of the first kind, and the latter is given by $\Delta\hat{p}_{B_s} = 2/D$. In figure 8, we plot with the solid and dashed line, respectively, D and the flow-induced change in the reduced bubble pressure defined as $\delta\hat{p}_B \equiv (p_{B_s} - p_{B_0})/(\mu k) = \delta\hat{p}_{B_s} - 1/Ca_s$, against the capillary number Ca_s in the regime where steady shapes can be found. The upper branch of the deformation parameter graph and the lower branch of the pressure graph above or below the turning points correspond to the unstable highly eccentric elongated shapes.

Tanveer & Vasconcelos (1995) showed that, as in the case of simple shear flow, the transient deformation of an incompressible circular bubble occurs through a sequence of elliptical shapes, and derived an ordinary differential equation governing the evolution of the bubble axes ratio. Because of the constraint of constant bubble area, the bubble pressure changes during the deformation according to an equation of state. Figure 9(a) shows a sequence of stages in the deformation of a bubble under constant area, for capillary number $Ca_0 = Ca_s = 0.300$ computed using the boundary

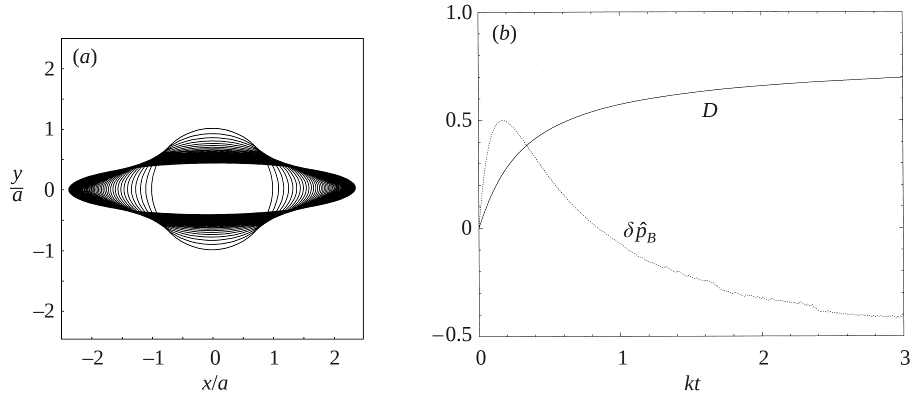

FIGURE 9. (*a*) Stages in the deformation of an incompressible bubble in purely elongational flow, for capillary number $Ca_0 = Ca_s = \mu ka/\gamma = 0.3$; (*b*) corresponding evolution of the deformation parameter (solid line) and change in bubble pressure (dotted line).

integral method, corresponding to the vertical dotted line in figure 8. Figure 9(*b*) displays the evolution of the deformation parameter (solid line) and change in bubble pressure expressed by $\delta\hat{p}_B$ (dotted line). The deformation of the free surface leads to a stationary shape corresponding to the lower branch of the deformation graph shown in figure 8. The evolution of the bubble pressure is similar to that described in § 5 for a bubble in simple shear flow, suggesting that a compressible bubble is expected to expand when it reaches the steady state.

This prediction is corroborated by numerical simulations. Figure 10 shows the evolution of the deformation parameter (solid line), reduced bubble area shifted by one unit (dashed line), and reduced rate of expansion (dotted line), for $Ca_0 = 0.300$ and $\hat{p}_\infty = 1$. By the end of the simulation, the bubble has expanded by nearly 5%, and this has raised the capillary number barely outside the regime where steady shapes can be found. In this extreme case, the expansion of the bubble has a destabilizing influence on the deformation.

7. Discussion

We have studied the behaviour of the bubble pressure and the effect of bubble compressibility in three complementary types of two-dimensional Stokes flow: shrinkage, shearing, and pure deformation. The results have shown that a bubble may contract or expand due to ambient fluid motion. In the case of shear and elongational flow, the bubble expands by a small percentage when it reaches a steady state, but the effect is significant only when the ambient pressure is less than, or comparable with, the capillary pressure due to surface tension.

Consideration of the two-dimensional flow was necessitated by the availability of numerical methods for computing the bubble pressure in terms of strongly singular integrals originating from the boundary-integral representation. Numerical methods for evaluating with sufficient accuracy analogous integrals in the more realistic case of three-dimensional flow are not available. Similarities in the structure of viscous flow past two- or three-dimensional drops and bubbles noted by previous authors, however, suggest that three-dimensional compressible bubbles are also expected to expand when subjected to an ambient shear or elongational flow. Earlier studies have shown that three-dimensional bubbles suspended in simple shear flow are unable to

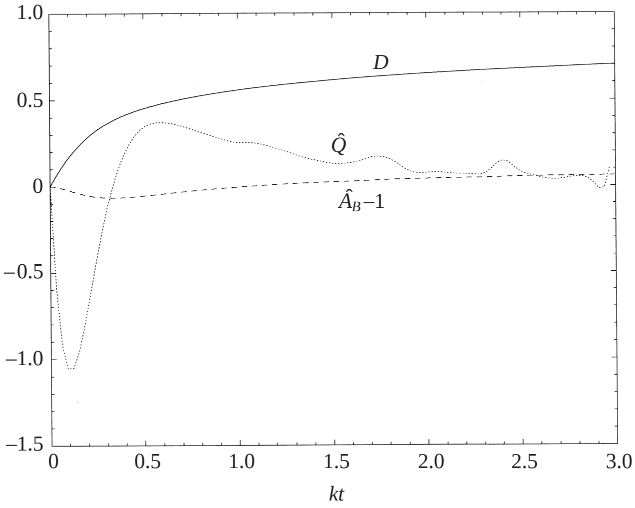

FIGURE 10. Evolution of a compressible bubble in purely elongational flow, for $Ca_0 = 0.3$ and $\hat{p}_\infty = 1$.

obtain a stationary shape when the capillary number exceeds a critical threshold (e.g. Kennedy, Pozrikidis & Skalak 1994), whereas two-dimensional bubbles obtain stationary shapes at all capillary numbers (Richardson 1968), as discussed in §4. The difference may be attributed to the Rayleigh capillary instability that destabilizes elongated three-dimensional shapes. In the case of three-dimensional shear flow, flow-induced expansion may raise the capillary number above the critical threshold and thus destabilize the free surface.

Consider the shear or elongational flow of a dilute suspension of compressible bubbles with a position-dependent shear rate or rate of expansion. In the absence of a constraint on the total volume of the suspension, the individual bubble volume and thus the bubble volume fraction is expected to develop spatial non-uniformities due to the uneven expansion of the bubbles, especially in regions of low pressure. In the case of internal flow occurring, for example, in a cavity or closed channel confined on all sides by rigid walls, bubble expansion is prohibited by the constraint of constant total flow volume, and the pressure in the liquid far from the bubble must increase or decrease so that the bubble volume and pressure remain constant and the rate of expansion vanishes during the deformation. Consequently, the liquid pressure in a cone-and-plate viscometer filled with a Newtonian liquid that contains bubbles is expected to increase by a small amount on raising the shear rate. This uniform increase contributes an osmotic-like pressure to the effective stress tensor of the suspension, and affects the normal stress differences indirectly through changes in the capillary number defined with respect to the bubble size at steady state.

This research was supported by a grant provided by the National Science Foundation.

REFERENCES

BLAKE, J. R. & GIBSON, D. C. 1987 Cavitation bubbles near boundaries. *Ann. Rev. Fluid Mech.* **19**, 99–123.

Boulton-Stone, J. M. 1995 The effect of surfactant on bursting gas bubbles. *J. Fluid Mech.* **302**, 231–257.

Christov, C. I. & Volkov, P. K. 1985 Numerical investigation of the steady viscous flow past a stationary deformable bubble. *J. Fluid Mech.* **158**, 341–364.

Kang, I. S. & Leal, L. G. 1987 Numerical solution of axisymmetric, unsteady free-boundary problems at finite Reynolds number. I. Finite-difference scheme and its applications to the deformation of a bubble in a uniaxial straining flow. *Phys. Fluids* **30**, 1929–1940.

Kennedy, M., Pozrikidis, C. & Skalak, R. 1994 Motion and deformation of liquid drops, and the rheology of dilute emulsions in shear flow. *Computers Fluids* **23**, 251–278.

Miksis, M. J. 1981 A bubble in an axially symmetric shear flow. *Phys Fluids* **24**, 1229–1231.

Plesset, M. S. & Prosperetti, A. 1977 Bubble dynamics and cavitation. *Ann. Rev. Fluid Mech.* **9**, 145–185.

Pozrikidis, C. 1992 *Boundary Integral and Singularity Methods for Linearized Viscous Flow*. Cambridge University Press.

Prosperetti, A. 1999 Old-fashioned bubble dynamics. In *Sonochemistry and Sonoluminescence* (ed. L. A. Crum, T. J. Mason, J. L. Reisse & K. S. Suslick). Kluwer.

Richardson, S. 1968 Two-dimensional bubbles in slow viscous flow. *J. Fluid Mech.* **33**, 476–493.

Ryskin, G. & Leal, L. G. 1984 Numerical solution of free-boundary problems in fluid mechanics. Part 1. The finite-difference method. *J. Fluid Mech.* **148**, 1–17.

Sangani, A. S. & Didwania, A. K. 1993 Dynamic simulations of flows of bubbly liquids at large Reynolds numbers. *J. Fluid Mech.* **250**, 307–337.

Sladek, V. & Sladek, J. 1998 *Singular Integrals in Boundary Element Methods.* Computational Mechanics Publications, Southampton.

Takagi, S., Prosperetti, A. & Matsumoto, Y. 1994 Drag coefficient of a gas bubble in an axisymmetric shear flow. *Phys. Fluids* **6**, 3186–3188.

Tanveer, S. & Vasconcelos, G. L. 1995 Time-evolving bubbles in two-dimensional Stokes flow. *J. Fluid Mech.* **301**, 325–344.

Yuan, H. & Prosperetti, A. 1994 On the in-line motion of two spherical bubbles in a viscous fluid. *J. Fluid Mech.* **278**, 325–349.